RSC Advances

PAPER

View Article Online
View Journal | View Issue

Cite this: *RSC Adv.*, 2022, **12**, 30322

Anisotropic dependence of radiation from excitons in Ga_2O_3/MoS_2 heterostructure†

Zexiang Deng *

Received 29th September 2022
Accepted 17th October 2022

DOI: 10.1039/d2ra06139b

rsc.li/rsc-advances

The anisotropic dependence of radiation arising from exciton recombination in the Ga_2O_3/MoS_2 heterostructure is investigated, using density functional theory and the Bethe–Salpeter equation. The wurtzite (WZ) and zinc blende (ZB) structures of the Ga_2O_3 monolayer with ferroelectric (FE) properties are assembled with a MoS_2 monolayer. Projected band structure, charge transfer and life time of excitons are discussed, to analyze which transition may be important to the creation of excitons from the electron–hole pair. A general formula of the angle-dependent intensities of radiation is derived. The characteristics of angle-dependent intensities that are closely related to the dipole moment of excitons are discussed, from the viewpoint of in-plane and out-of-plane polarizations. These predictions on radiation of the Ga_2O_3/MoS_2 heterostructure should guide exciton dynamics in low dimensional systems and rational design of optoelectronic devices.

1 Introduction

The applications of deep-ultraviolet photodetectors have made great progress in recent years. As one of the ultra-wide band gap (4.6–4.9 eV)[1,2] materials, gallium oxide (Ga_2O_3) has very unique electronic and optical properties, which make it suitable to be the building blocks of solar-blind photodetectors[3–6] and power devices.[7,8] According to different crystal structures, it can be classified as five different polymorphs (α, β, γ, δ, ε).[9–11]

Among them, the stable β-Ga_2O_3 based semiconductor materials, are suitable for applications in next-generation power electronic and optoelectronic devices. It is reported that Schottky interfaces based on β-Ga_2O_3 can realize a large Schottky barrier height, which makes high-temperature operation possible.[12] A vertical-type Schottky photodetector based on a (100)-oriented β-Ga_2O_3 substrate has been fabricated with simple processes of thermal annealing and vacuum evaporation.[13] Optoelectronic analysis reveals that the heterojunction device is virtually blind to light illumination with wavelength longer than 280 nm, assembled by coating multilayer graphene on β-Ga_2O_3 wafer.[14] Self-powered solar-blind photodetectors based on diamond/β-Ga_2O_3 heterojunctions have been fabricated successfully. These photodetectors can exhibit repeatability and stability without any external power supply.[15] What's more, a deep UV photodiode is fabricated using a heterojunction between β-Ga_2O_3 and GaN. The response time of the photodiode is in the order of sub-milliseconds.[16]

Besides the bulk β-Ga_2O_3, with the rapidly growing synthesis technology in recent years, as one of the building blocks of functional devices, the two-dimensional (2D) van der Waals materials have been regarded as a promising material for the breathtaking through of nanotechnology and its applications. β-Ga_2O_3 films are grown on $SrTiO_3$ (100) substrate by a high-vacuum MOCVD system.[17] As the similar way in graphene, mechanical exfoliation of the bulk β-Ga_2O_3 by using an adhesive tape is followed by plasma etching to tune its thickness.[18] Feng *et al.* report the successful fabrication of 2D Ga_2O_3 from the corresponding GaSe nanosheets and a solar blind photodetector based on 2D Ga_2O_3. The as-prepared 2D β-Ga_2O_3 is polycrystalline and has a thickness of less than 10 nm.[19] As its unusual asymmetrical structure of 2D Ga_2O_3, by using selected surface orientations, improving the selectivity and sensitivity of gas sensors and release controlled by a ferroelectric switch become possible.[20–22] Meng *et al.* predict a stable hexagonal phase of 2D Ga_2O_3 and In_2O_3, by using a global searching method based on an evolutionary algorithm, combined with density functional theory (DFT) simulations.[23]

The devices based on van der Waals heterostructures widely broaden the applications of these 2D ferroelectric materials. *E.g.* high breakdown electric field in β-Ga_2O_3/graphene vertical barrister heterostructure.,[24] Ga_2O_3/GaN heterostructural ultraviolet photodetectors,[25] deep-ultraviolet photodetection using single-crystalline β-Ga_2O_3/NiO heterojunctions,[26] ultrahigh deep-UV sensitivity in graphene-gated β-Ga_2O_3 phototransistors,[3] and $PdCoO_2$/β-Ga_2O_3 Schottky diodes for high-temperature operation.[12]

Another emerging 2D semiconductors with a sizable direct bandgap and novel physical properties are monolayer group VI transition metal dichalcogenides (TMDs).[27–30] Both theoretically

School of Science, Guilin University of Aerospace Technology, Guilin 541004, People's Republic of China. E-mail: dengzex@mail2.sysu.edu.cn

† Electronic supplementary information (ESI) available. See DOI: https://doi.org/10.1039/d2ra06139b

and experimentally, light emitting devices based on TMDs have been demonstrated low threshold.[29] WSe_2, WS_2, $MoSe_2$ and MoS_2 monolayers can be flexibly exfoliated onto the same SiO_2/Si substrate,[31] which makes it suitable to be the building blocks of heterostructures.

Based on In_2Se_3 and other III_2–VI_3 van der Waals materials, using first-principles calculations, Ding *et al.* discover a branch of the 2D materials family, which exhibits room-temperature ferroelectricity (FE) with reversible spontaneous electric polarization in both out-of-plane and in-plane orientations.[32] In addition, a novel 2D Ga_2O_3 monolayer is constructed and systematically investigated by first-principles calculations. The 2D Ga_2O_3 monolayer has an asymmetric configuration with a quintuple-layer (QL) atomic structure, the same as the well-studied α-In_2Se_3,[32] and is expected to be experimentally synthesized.[33] What's more, the mismatch of crystal lattice between Ga_2O_3 and MoS_2 monolayer is less than 3%.[32,34,35]

In material engineering, one of the difficult task is combining the best of different ingredients into one ultimate device. Thereby, in this study, we propose a model of Ga_2O_3/MoS_2 heterostructure, using DFT and Bethe–Salpeter equation.[36–38] The wurtzite (WZ) and zinc blende (ZB) structures of Ga_2O_3 monolayer with ferroelectric (FE) properties are assembled with MoS_2 monolayer. The projected band structure and charge transfer are discussed, and explain the life time of radiation from exciton recombination. The angle-dependent intensities of radiation are derived, which is general and can be applied to other similar systems. Finally, the characteristics of angle-dependent intensities including in-plane and out-of-plane polarization, are presented, which can be measured in future experiments.

2 Methods

According to the Fermi's golden rule, the transition from excited state $|S\rangle$ to ground state $|G\rangle$, arising from the electron–photon interaction H^{int} can be written as,

$$\gamma = \frac{2\pi}{\hbar}|\langle G|H_{\text{int}}|S\rangle|^2\delta(E_{\text{S}} - \hbar\omega_{\text{k}}) \tag{1}$$

where γ represents the rate of emission of a photon with angular frequency ω_{k}, and E_{S} is the exciton energy. The Hamiltonian describing the electron–photon interaction can be expressed as,[39]

$$H_{\text{int}} = -\frac{e}{m}\int \mathrm{d}\mathbf{r}\psi^{\dagger}(\mathbf{r})\mathbf{A}(\mathbf{r})\cdot\mathbf{p}\psi(\mathbf{r}) \tag{2}$$

where $\mathbf{p}$ is the electron momentum operator and the vector-potential operator $\mathbf{A}(\mathbf{r})$ is,[40]

$$\mathbf{A}(\mathbf{r}) = \sum_{\mathbf{k}}\sum_{\lambda=1,2}\sqrt{\frac{\hbar}{2\varepsilon_0 V\omega_{\text{k}}}}\boldsymbol{e}_{\mathbf{k}\lambda}\left[a^{\dagger}_{\mathbf{k}\lambda}\mathrm{e}^{-i\mathbf{k}\cdot\mathbf{r}} + \text{h.c.}\right]. \tag{3}$$

where $\hat{a}^{\dagger}_{\mathbf{k}\lambda}$ and $\hat{a}_{\mathbf{k}\lambda}$ denote the creation and annihilation operators for a phonon of with momentum $\mathbf{k}$ and vibrating direction $\boldsymbol{e}_{\lambda}$. With the relation between operators $\mathbf{r}$ and $\mathbf{p}$ ($\mathbf{p} = -\mathrm{i}m/\hbar[\mathbf{r}, H]$), inserting eqn (3) into (2), the rate in eqn (1) can be written as,

$$\gamma = \frac{{E_{\text{S}}}^3 e^2}{8\pi^2\hbar^4\varepsilon_0 c^3}\sum_{\lambda=1,2}\int \mathrm{d}\Omega|\boldsymbol{e}_{\mathbf{k}\lambda}\cdot\langle G|\mathbf{r}|S\rangle|^2 \tag{4}$$

In general, the unit vector of light propagating direction can be set as $\boldsymbol{e}_{\mathbf{k}} = (\sin\theta\cos\phi, \sin\theta\sin\phi, \cos\theta)$. As the intensity of emitting light with a given angle is proportional to the rate of radiation, eqn (5) can provide angle-dependent polar plots of the photoluminescence (PL) spectroscopy in experiments. Furthermore, the contributions of intensity can be measured experimentally in in-plane (IP) and out-of-plane (OP) directions, respectively, as shown in eqn (6). The rate γ of radiation can be expressed as,

$$\gamma = \gamma_0\int \mathrm{d}\Omega\, Y(\theta,\ \phi), \quad \gamma_0 = \frac{{E_{\text{S}}}^3 e^2\mu^2}{8\pi^2\hbar^4\varepsilon_0 c^3}. \tag{5}$$

Here, $\int \mathrm{d}\Omega = \int \sin\theta \mathrm{d}\theta\mathrm{d}\phi$ is the integral over solid angle. γ_0 is the rate constant independent of radiation angles, with $\boldsymbol{\mu} = \langle G|\mathbf{r}|S\rangle$. And the angle-dependent function $Y(\theta, \phi)$ is denoted as,

$$Y(\theta,\ \phi) = \sum_{\lambda}\left|\boldsymbol{e}_{\mathbf{k}\lambda}\cdot\boldsymbol{e}_{\boldsymbol{\mu}}\right|^2 = Y_{\text{IP}}(\theta,\ \phi) + Y_{\text{OP}}(\theta,\ \phi), \tag{6}$$

with the unit vector of in-plane polarization $\boldsymbol{e}_{\text{IP}} = (\sin\phi, -\cos\phi, 0)$ and the unit vector of out-of-plane polarization $\boldsymbol{e}_{\text{OP}} = (\cos\theta\cos\phi, \cos\theta\sin\phi, -\sin\theta)$.

Finally, the difficulty is to evaluate $|\langle G|\mathbf{r}|S\rangle|$, which is closely related to the dipole moment of exciton. Based on the expansion coefficient $A^{\text{S}}_{mn\mathbf{k}}$ by solving the Bethe–Salpeter equation (BSE), implemented in the BerkeleyGW codes,[36–38] the wave function of an exciton is expressed as a linear combinations of electron–hole transitions,

$$|S\rangle = \sum_{mn\mathbf{k}} A^{\text{S}}_{mn\mathbf{k}}\hat{c}^{\dagger}_{m\mathbf{k}}\hat{c}_{n\mathbf{k}}|0\rangle \tag{7}$$

where $\hat{c}^{\dagger}_{n\mathbf{k}}$ and $\hat{c}_{n\mathbf{k}}$ denote the creation and annihilation operators for an electron in the n-th electronic state with momentum $\mathbf{k}$. The indices m and n run over all the conduction and valence bands, respectively. Overall, with the exciton wave function, the dipole moment of exciton can be obtained. The detail derivatives of the above equations can be found in the ESI.†

3 Results and discussions

In this study, two kinds of Ga_2O_3 monolayers with ferroelectric (FE-WZ and FE-BZ) phases are included. As shown in Fig. 1b and c, these two structures with five-atomic-layers QL stacking, are demonstrated stable in In_2Se_3.[32] In addition, it is necessary to considering the conventional 'lattice mismatch' issue, when constructing vertical heterostructures using different 2D materials. The optimized lattice parameters of FE-ZB Ga_2O_3 are a = 3.08 Å with GGA-PBE.[33] For the bulk MoS_2, the lattice parameter is a = 3.16 Å,[41,42] which means that the mismatch rate of MoS_2 and Ga_2O_3 monolayers should be less than 3%. The energy-distance (between MoS_2 and Ga_2O_3 monolayer) curve is also plotted in Fig. 1a. In our calculations, the distance for the

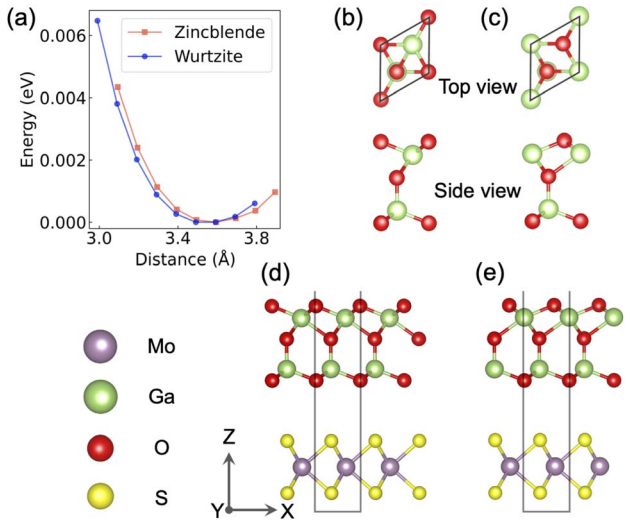

Fig. 1 (a) Energy-distance (between MoS_2 and Ga_2O_3 monolayer) curve for FE-ZB/MoS_2 and FE-WZ/MoS_2 heterostructure, marked with red and blue point line, respectively. Top and side view crystal structure of FE-ZB (b) and FE-WZ (c) Ga_2O_3 monolayer. Side view of FE-ZB/MoS_2 (d) and FE-WZ/MoS_2 (e) heterostructure. The red, green, violet and yellow balls denote O, Ga, Mo and S atoms, respectively.

relaxed FE-ZB/MoS_2 (Fig. 1d) and FE-WZ/MoS_2 (Fig. 1e) heterostructures are 3.58 Å and 3.51 Å, respectively.

3.1 Electronic structures and crystal stability

Before the investigations of excited states, it is necessary to understand the electronic structures from the viewpoint of DFT. To better study the electronic structure of Ga_2O_3/MoS_2 heterostructures, the atom-projected band structures and partial density of states (PDOS) for both FE-ZB/MoS_2 and FE-WZ/MoS_2 heterostructures are exhibited in Fig. 2. As reported in previous literature, both FE-ZB and FE-WZ Ga_2O_3 monolayers have indirect band gaps. For the FE-ZB/MoS_2 heterostructure, it is still an indirect-band-gap semiconductor, the minimum of conduction band (CBM) locates at Γ point, while the maximum of valence band (VBM) locates at K point. In the FE-WB/MoS_2 heterostructure, both CBM and VBM locate at K point, which make it a direct-band-gap semiconductor with smaller gaps. We notice that, in the Ga_2O_3/MoS_2 heterostructure, the predominant contribution of the conduction band comes from Mo atoms of MoS_2, while for the valence band, the oxygen atoms of Ga_2O_3 make the main contribution. This point can also be verified by the corresponding PDOS in the right panel of Fig. 2. This means that, in this Ga_2O_3/MoS_2 heterostructures, it seems that, the electron should lie in the conduction band of MoS_2, while the hole should come from the valence band in Ga_2O_3. To verify the stability of the heterostructure, the phonon band structures are presented in Fig. 3. We notice that there are totally 24 phonon branches, as there are 8 atoms in the unit cell. In the plot of phonon band, the absence of imaginary phonon modes indicates that, the crystal structure of the heterostructure of FE-ZB/MoS_2 and FE-WZ/MoS_2 heterostructures could be dynamically stable.

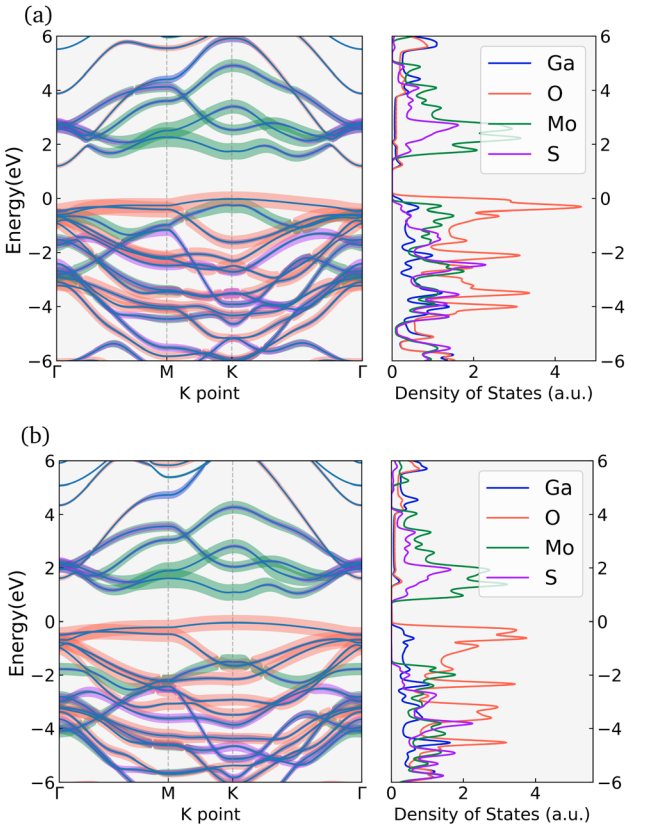

Fig. 2 Band structure and PDOS of (a) FE-ZB/MoS_2 and (b) FE-WZ/MoS_2 heterostructures. The maximum of valence band (VBM) is set at zero. Atom-projected band structures and PDOS are highlighted with red, green, violet and yellow colors for O, Ga, Mo and S elements, respectively.

3.2 Charge transfer and life time

As is known to all, the formation of exciton is closely related to the electron–hole pairs, which can be reflected by the distribution of charge density in the heterostructure and its interface. The charge density difference $\Delta\rho$ is defined as:

$$\Delta\rho = \rho_{\text{all}} - \rho_{\text{Ga}_2\text{O}_3} - \rho_{\text{MoS}_2} \quad (8)$$

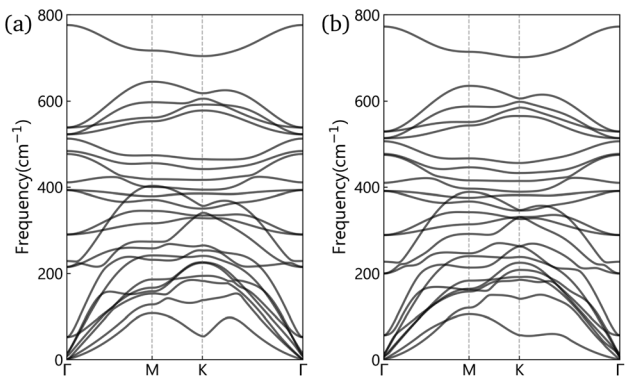

Fig. 3 Phonon band structure of (a) FE-ZB/MoS_2 and (b) FE-WZ/MoS_2 heterostructures.

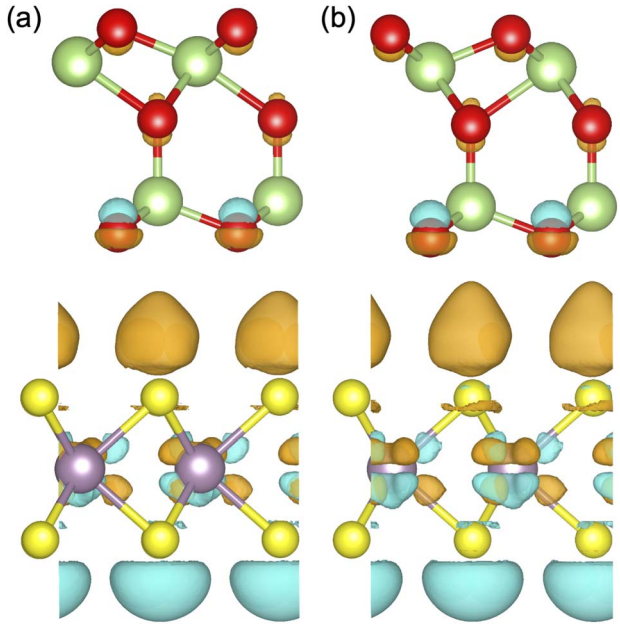

Fig. 4 Side view of calculated charge density difference of (a) FE-ZB/MoS_2 and (b) FE-WZ/MoS_2 heterostructures. The yellow and cyan colors represent charge accumulation and loss, respectively.

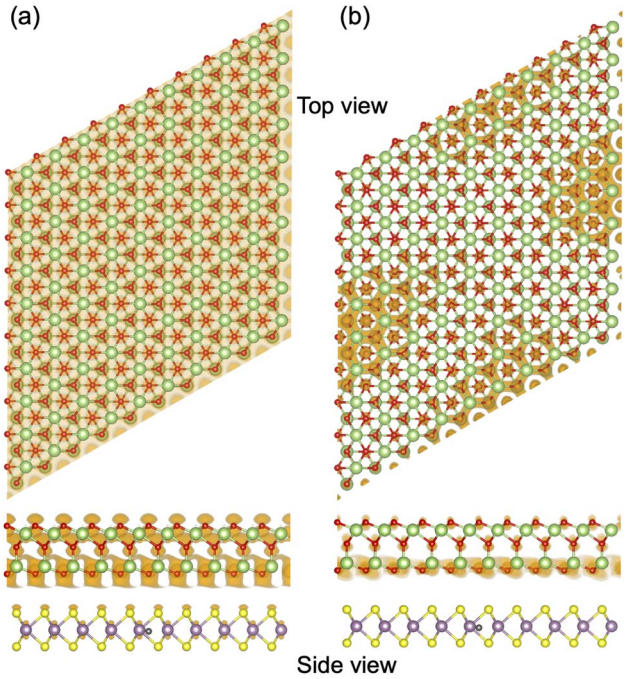

Fig. 5 Top and side view of calculated exciton wave functions of FE-ZB/MoS_2 heterostructures for the lowest-energy S_1 (a) and second-lowest S_2 (b) exciton states. The position of hole is fixed in the center of MoS_2 monolayer of the heterostructure. The wave function is visualized in a supercell of 10 × 10.

where ρ_{all} represents the charge density of the G_2O_3/MoS_2 heterostructure, while $\rho_{Ga_2O_3}$ and ρ_{MoS_2} denote the charge density of G_2O_3 and MoS_2 monolayers, respectively. From the side view of charge density difference in Fig. 4, the charge transfer mainly happens in MoS_2 monolayer. The charge moves from the outside part of MoS_2, and accumulates in the interface, near the inside part of MoS_2. Compared with MoS_2, the charge density difference of G_2O_3 monolayer changes very little, and mainly happens on the lowest oxygen layer, close to the interface.

As a supplement to the charge density difference, the exciton wave functions are provided. Taking the Tamm–Dancoff approximation by considering only valence to conduction band transitions, the wave function in real space can be expressed as:[38]

$$\psi(\boldsymbol{r}_e,\ \boldsymbol{r}_h) = \sum_{cv\mathbf{k}} A^S_{mn\mathbf{k}} \psi^*_{v\mathbf{k}}(\boldsymbol{r}_h)\psi_{c\mathbf{k}}(\boldsymbol{r}_e). \quad (9)$$

Here, $\boldsymbol{r}_e$ and $\boldsymbol{r}_h$ denote the position of electron and hole in an electron–hole pair. As shown in Fig. 5, the wave function of exciton mainly locates on the Ga_2O_3 monolayer, in both the lowest-energy S_1 and second-lowest S_2 exciton states. This point is demonstrated by the charge density difference $\Delta\rho$, which happens mostly in the same monolayer of the heterostructure, rather than interlayer. Compared with the flat and spreading status of S_1, the wave function of S_2 appears much more localized, with two accumulation center in the supercell of 10 × 10.

The radiative life time $(1/\gamma)$ of the lowest S_1 and second S_2 lowest-energy excited states for FE-ZB/MoS_2 and FE-WZ/MoS_2 heterostructures are summarized in Table 1. The radiation of exciton is closely related to the lower-energy bright states. In our Ga_2O_3/MoS_2 heterostructure, the S_1 is nondegenerate, while S_2 and S_3 are doubly degenerate. As comparison, the lowest-energy

Table 1 The radiative lifetime $(1/\gamma)$ of FE-ZB/MoS_2 and FE-WZ/MoS_2 heterostructures

System	E_S (eV)	Lifetime (ns)
FE-ZB/MoS_2	S_1 (1.27)	554
FE-ZB/MoS_2	S_2 (2.00)	93
FE-WZ/MoS_2	S_1 (1.23)	519
FE-WZ/MoS_2	S_2 (1.95)	90

exciton states (S_1 and S_2) of Ga_2O_3 monolayer are doubly degenerate (for FE-ZB Ga_2O_3 monolayer $E_{S_1} = E_{S_2} = 3.15$ eV, for FE-WZ Ga_2O_3 monolayer $E_{S_1} = E_{S_2} = 3.38$ eV), which is related to the two equivalent K and K' points in the reciprocal lattice. Compared with the large exciton energy (more than 3.0 eV) in Ga_2O_3 monolayer, the energy of S_1 in the heterostructure is about 1.2–1.3 eV. And as the doubly degenerate property and larger exciton energy, the life time of S_2 (~90 ns) is much shorter than that of S_1 (~500 ns) in both FE-ZB/MoS_2 and FE-WZ/MoS_2 heterostructures. In spite that our calculation can not give exact quantitative results, it still can provide qualitative guidance in future experiments.

3.3 Angle dependence of radiation

To further understand the anisotropic radiation of exciton, the angle-dependent intensity is investigated, the results of which can be compared with that in experiments. In a polar coordinate system, the propagating direction of light with $\boldsymbol{k}$ vector can be written as, $\boldsymbol{e_k} = (\sin\theta\cos\phi, \sin\theta\sin\phi, \cos\theta)$, with polar angle θ

and azimuth angle ϕ. As shown in Fig. 1, the x and y axes are on the plane of MoS_2 and G_2O_3 monolayers. The polarization direction $\boldsymbol{e}_{\mathbf{k}\lambda}$ of the light can be expressed as the in-plane (IP) and out-of-plane (OP) unit vectors, with $\boldsymbol{e}_{\mathrm{IP}} = (\sin\phi, -\cos\phi, 0)$, and $\boldsymbol{e}_{\mathrm{OP}} = (\cos\theta\cos\phi,\ \cos\theta\sin\phi,\ -\sin\theta)$. In general, the contribution from IP and OP polarizations can be written as:

$$\gamma_{\mathrm{IP}}(\theta,\ \phi) = \gamma_0\left|\frac{\mu_x}{\mu}\sin\phi - \frac{\mu_y}{\mu}\cos\phi\right|^2, \quad (10)$$

$$\gamma_{\mathrm{OP}}(\theta,\ \phi) = \gamma_0\left|\frac{\mu_x}{\mu}\cos\theta\cos\phi + \frac{\mu_y}{\mu}\cos\theta\sin\phi - \frac{\mu_z}{\mu}\sin\theta\right|^2. \quad (11)$$

Fig. 6 shows the polar plots of the angle-dependent intensities for radiation of the lowest-energy exciton, with specific polar angle (θ = 0, 45, 135° for FE-ZB/MoS_2 and FE-WZ/MoS_2 heterostructure, respectively. We notice that, for the intensity of IP polarization, it does not depend on the polar angle θ, only the function of azimuth angle ϕ. Both IP and OP intensities have two maxima, the connecting line of which are perpendicular to each other. When $\theta = 0°$, the total intensity is isotropic, which means that the two contributions from IP and OP are equal. As shown in eqn (11), when the polar angle $\theta = 0°$, there is no contribution from z direction, which means that the OP polarization lies on the x–y plane, as the IP polarization dose. When the polar angle $\theta = 45°$ (Fig. 6c and d), for the OP polarization, the intensity of one maximum is much larger than another one. Thus, the total intensity is anisotropic, obviously depending on the azimuth angle ϕ. When the polar angle $\theta = 135°$ (Fig. 6e and f), the configuration of radiation is similar, but the position of maxima just simply reversed. For FE-ZB/MoS_2 and FE-WZ/MoS_2 heterostructures, their configuration of radiation are similar, and the main difference comes from the locations of maxima. From eqn (10) and (11), we notice that, the maxima of intensities depend on the dipole moment vector, which can be demonstrated by experiments. In other words, the radiation of IP and OP polarizations can be measured in experiments. With these configurations of radiation, the dipole moment of exciton can be measured indirectly.

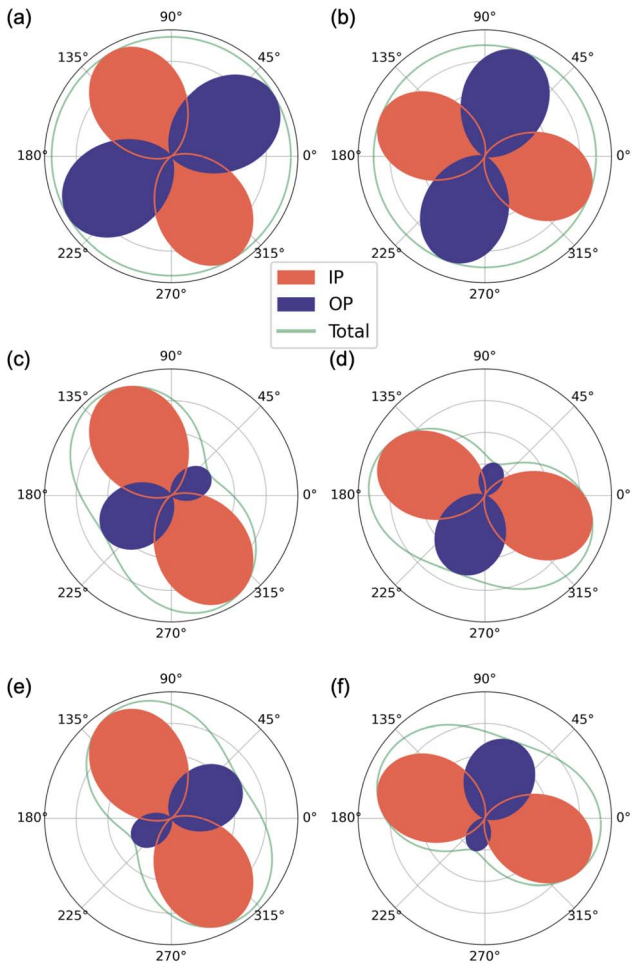

Fig. 6 Polar plots of the angle-dependent intensities for radiation of the lowest-energy exciton (S_1), with specific polar angle θ [for (a and b), $\theta = 0°$, for (c and d), $\theta = 45°$, for (e and f), $\theta = 135°$]. The left (a, c and e) and right (b, d and f) panels are for FE-ZB/MoS_2 and FE-WZ/MoS_2 heterostructures, respectively. The maximum scale range of the intensities in the polar plots is 2×10^{-3} ns^{-1}.

4 Conclusions

We have investigated the anisotropic dependence of radiation arising from exciton recombination in Ga_2O_3/MoS_2 heterostructure, using density functional theory and Bethe–Salpeter equation. The FE-ZB and FE-WZ structures of Ga_2O_3 monolayer with ferroelectric properties are assembled with MoS_2 monolayer. From the projected band structure, we find that the predominant contribution of the conduction band comes from Mo atoms of MoS_2, while for the valence band, the oxygen atoms of Ga_2O_3 make the main contribution. The charge transfer and wave function of exciton reveal that, the charge density difference happens mainly in the same monolayer of the heterostructure. The life time of doubly degenerate S_2 (~90 ns) is much shorter than that of S_1 (~500 ns) in both FE-ZB/MoS_2 and FE-WZ/MoS_2 heterostructures. The characteristics of angle-dependent intensities are discussed. We find that, the maxima of intensity depend on the dipole moment vector, which can be demonstrated by experiments. These predictions on radiation of Ga_2O_3/MoS_2 heterostructure should guide rational design of optoelectronic devices in low dimensional systems.

Conflicts of interest

There are no conflicts of interest to declare.

Acknowledgements

This work was supported by the Guangxi Natural Science Foundation (Grant No. 2021GXNSFAA220129), the Project of Improving the Basic Scientific Research Ability of Young and Middle-aged Teachers in Universities of Guangxi (Grant No. 2022KY0784), the Foundation of Guilin University of Aerospace

Technology (Grant No. 2021BJXM019), the High-Performance Servers of Guilin University of Aerospace Technology.

Notes and references

1 S. Stepanov, V. Nikolaev, V. Bougrov and A. Romanov, *Rev. Adv. Mater. Sci.*, 2016, **44**, 63–86.
2 K. A. Mengle, G. Shi, D. Bayerl and E. Kioupakis, *Appl. Phys. Lett.*, 2016, **109**, 212104.
3 S. Kim, S. Oh and J. Kim, *ACS Photonics*, 2019, **6**, 1026–1032.
4 S. Pearton, J. Yang, P. H. Cary IV, F. Ren, J. Kim, M. J. Tadjer and M. A. Mastro, *Appl. Phys. Rev.*, 2018, **5**, 011301.
5 H. Chen, K. Liu, L. Hu, A. A. Al-Ghamdi and X. Fang, *Mater. Today*, 2015, **18**, 493–502.
6 L. Sang, M. Liao and M. Sumiya, *Sensors*, 2013, **13**, 10482–10518.
7 K. Arora, N. Goel, M. Kumar and M. Kumar, *ACS Photonics*, 2018, **5**, 2391–2401.
8 W. Guo, Y. Guo, H. Dong and X. Zhou, *Phys. Chem. Chem. Phys.*, 2015, **17**, 5817–5825.
9 D. Kaur and M. Kumar, *Adv. Opt. Mater.*, 2021, **9**, 2002160.
10 J. Zhang, J. Shi, D.-C. Qi, L. Chen and K. H. Zhang, *APL Mater.*, 2020, **8**, 020906.
11 T. Gake, Y. Kumagai and F. Oba, *Phys. Rev. Mater.*, 2019, **3**, 044603.
12 T. Harada, S. Ito and A. Tsukazaki, *Sci. Adv.*, 2019, **5**, eaax5733.
13 T. Oshima, T. Okuno, N. Arai, N. Suzuki, S. Ohira and S. Fujita, *Appl. Phys. Express*, 2008, **1**, 011202.
14 W.-Y. Kong, G.-A. Wu, K.-Y. Wang, T.-F. Zhang, Y.-F. Zou, D.-D. Wang and L.-B. Luo, *Adv. Mater.*, 2016, **28**, 10725–10731.
15 Y.-C. Chen, Y.-J. Lu, C.-N. Lin, Y.-Z. Tian, C.-J. Gao, L. Dong and C.-X. Shan, *J. Mater. Chem. C*, 2018, **6**, 5727–5732.
16 S. Nakagomi, T.-a. Sato, Y. Takahashi and Y. Kokubun, *Sens. Actuators, A*, 2015, **232**, 208–213.
17 D. Wang, X. Ma, H. Xiao, R. Chen, Y. Le, C. Luan, B. Zhang and J. Ma, *Mater. Res. Bull.*, 2021, 111718.
18 Y. Kwon, G. Lee, S. Oh, J. Kim, S. J. Pearton and F. Ren, *Appl. Phys. Lett.*, 2017, **110**, 131901.
19 W. Feng, X. Wang, J. Zhang, L. Wang, W. Zheng, P. Hu, W. Cao and B. Yang, *J. Mater. Chem. C*, 2014, **2**, 3254–3259.
20 J. Zhao, X. Huang, Y. Yin, Y. Liao, H. Mo, Q. Qian, Y. Guo, X. Chen, Z. Zhang and M. Hua, *J. Phys. Chem. Lett.*, 2021, **12**, 5813–5820.
21 C. Jin, X. Tang, X. Tan, S. C. Smith, Y. Dai and L. Kou, *J. Mater. Chem. A*, 2019, **7**, 1099–1106.
22 X. Tang, J. Shang, Y. Gu, A. Du and L. Kou, *J. Mater. Chem. A*, 2020, **8**, 7331–7338.
23 R. Meng, M. Houssa, K. Iordanidou, G. Pourtois, V. Afanasiev and A. Stesmans, *J. Appl. Phys.*, 2020, **128**, 034304.
24 X. Yan, I. S. Esqueda, J. Ma, J. Tice and H. Wang, *Appl. Phys. Lett.*, 2018, **112**, 032101.
25 R. Tang, G. Li, Y. Jiang, N. Gao, J. Li, C. Li, K. Huang, J. Kang, T. Wang and R. Zhang, *ACS Appl. Electron. Mater.*, 2021, **4**, 188–196.
26 K.-H. Li, N. Alfaraj, C. H. Kang, L. Braic, M. N. Hedhili, Z. Guo, T. K. Ng and B. S. Ooi, *ACS Appl. Mater. Interfaces*, 2019, **11**, 35095–35104.
27 K. F. Mak, C. Lee, J. Hone, J. Shan and T. F. Heinz, *Phys. Rev. Lett.*, 2010, **105**, 136805.
28 Q. H. Wang, K. Kalantar-Zadeh, A. Kis, J. N. Coleman and M. S. Strano, *Nat. Nanotechnol.*, 2012, **7**, 699–712.
29 X. Meng, R. R. Grote, W. Jin, J. I. Dadap, N. C. Panoiu and R. M. Osgood, *Opt. Lett.*, 2016, **41**, 2636–2639.
30 K. Novoselov, o. A. Mishchenko, o. A. Carvalho and A. Castro Neto, *Science*, 2016, **353**, aac9439.
31 J. Jadczak, J. Kutrowska-Girzycka, P. Kapuściński, Y. Huang, A. Wójs and z. Bryja, *Nanotechnology*, 2017, **28**, 395702.
32 W. Ding, J. Zhu, Z. Wang, Y. Gao, D. Xiao, Y. Gu, Z. Zhang and W. Zhu, *Nat. Commun.*, 2017, **8**, 1–8.
33 Y. Liao, Z. Zhang, Z. Gao, Q. Qian and M. Hua, *ACS Appl. Mater. Interfaces*, 2020, **12**, 30659–30669.
34 J. Yu, C. Xia, Z. Hu, X. Hao, L. Wang, Q. Fang, *et al.*, *Phys. Chem. Chem. Phys.*, 2022, **24**, 3289–3295.
35 C. Adessi, S. Pecorario, S. Thebaud and G. Bouzerar, *Phys. Chem. Chem. Phys.*, 2020, **22**, 15048–15057.
36 M. S. Hybertsen and S. G. Louie, *Phys. Rev. B: Condens. Matter Mater. Phys.*, 1986, **34**, 5390.
37 M. Rohlfing and S. G. Louie, *Phys. Rev. B: Condens. Matter Mater. Phys.*, 2000, **62**, 4927.
38 J. Deslippe, G. Samsonidze, D. A. Strubbe, M. Jain, M. L. Cohen and S. G. Louie, *Comput. Phys. Commun.*, 2012, **183**, 1269–1289.
39 F. Wu, D. Rocca and Y. Ping, *J. Mater. Chem. C*, 2019, **7**, 12891–12897.
40 R. Loudon, *The Quantum Theory of Light*, Oxford University Press, 2000.
41 S. Balendhran, S. Walia, H. Nili, J. Z. Ou, S. Zhuiykov, R. B. Kaner, S. Sriram, M. Bhaskaran and K. Kalantar-zadeh, *Adv. Funct. Mater.*, 2013, **23**, 3952–3970.
42 S. Sugai and T. Ueda, *Phys. Rev. B: Condens. Matter Mater. Phys.*, 1982, **26**, 6554.